Source of Acquisition
NASA Glenn Research Center

E-8752

A NUMERICAL INVESTIGATION OF TURBULENT FLOW IN NONCIRCULAR DUCTS

Hsiao C. Kao
National Aeronautics and Space Administration
Lewis Research Center
Cleveland, Ohio 44135

SUMMARY

Since turbulent duct flows play an important role in engineering, continuous efforts to investigate this problem have been made. Until recently, these investigations were limited mostly to experiments and various semi-analytic methods. Owing to the improvement of turbulence modeling, the prevailing method of prediction is now mainly numerical. The majority of these studies deals, however, with turbulent flows in circular or square ducts and only limited information is available for straight noncircular ducts. In view of this situation, we propose to conduct a numerical investigation of turbulent flow in a class of ducts, whose cross sections vary from a circle to a near square. Turbulent flow in a noncircular duct is characterized by the presence of secondary flow for which a more refined turbulence model than the k-ε equations is required. In order to show that the calculated results are credible, various modes of verification were used to examine the results for a selected configuration, including an accuracy check by a scaling law and observing the decay of secondary flow as the cross section changes from a noncircular shape to a circle. After this was done, computations were performed for other configurations and with different Reynolds numbers from which wall shear stresses and friction factors are plotted.

Keywords: Numerical computation; Turbulent flow; Noncircular duct; Friction factor.

NOMENCLATURE

a^*	"radius" of super circle (Fig. 3)
d	dimensionless distance normal to wall, $d = d^*/a^*$
D_h^*	hydraulic diameter, $D_h^* = 4A^*/S^*$ (A^* = area, S^* = perimeter)
D_n	dimensionless pressure gradient, $D_n = -\frac{\partial p^*}{\partial x^*}\frac{a^*}{\rho^* U_b^{*2}}$
h_1, h_2	convariant metric coefficients
k	turbulent kinetic energy, $k = k^*/U_b^{*2}$
n	exponent of super circle (Eq. (1))
P	production rate of k
p	pressure, $p = p^*/\rho^* U_b^{*2}$
Re	reference Reynolds number, $Re = U_b^* a^*/\nu^*$
$\overline{Re}$	actual Reynolds number, $\overline{Re} = \overline{U}_b^* \overline{D}_h^*/\nu^*$
U,V,W	averaged velocity components in cartesian coordinates, $U = U^*/U_b^* \ldots W = W^*/U_b^*$
$\overline{U}_b$	$\overline{U}_b^*/U_b^*$
U_b^*	reference bulk velocity
$\overline{U}_b^*$	calculated (actual) bulk velocity
U_τ	friction velocity, $U_\tau = (\tau_w^*/\rho^*)^{1/2}/U_b^*$
$\hat{v}, \hat{w}$	contravariant velocity components (Fig. 3)
$\overline{v^2}, \ldots, \overline{vw}$	Reynolds stresses in cartesian coordinates, $\overline{v^2} = \overline{v^{*2}}/U_b^{*2}, \ldots \overline{vw} = \overline{v^* w^*}/U_b^{*2}$
x,y,z	cartesian coordinates, $x = x^*/a^* \ldots z = z^*/a^*$
ε	dissipation rate of k, $\varepsilon = \varepsilon^* a^*/U_b^{*3}$
ζ	wall coordinate, $\zeta = U_\tau^* d^*/\nu^* = Re\, U_\tau\, d$
λ	friction factors, $\lambda = 8\overline{\tau}_w^*/\rho^* \overline{U}_b^{*2}$
ν^*	kinematic viscosity
ν_t	dimensionless eddy viscosity, $\nu_t = \nu_t^*/\nu^*$
ξ, η	transformed coordinates
ρ^*	density

ϕ dimensionless streamwise velocity components, $\phi = U^*/U_\tau^*$ (Eq. (20))

τ_w^* local streamwise wall shear stress

$\bar{\tau}_w^*$ average streamwise wall shear stress

Superscript:

* dimensional quantity

1. INTRODUCTION

Since turbulent flow in straight noncircular ducts is of practical importance, a wealth of investigation exists. Most of these studies are either experimental or semi-analytic by means of correlations through equivalent hydraulic diameter. See, for example, Hartnett, Koh and McComas (1962), Aranovitch (1971), and Jones (1976) among many others. More recently numerical computations based on turbulence models have been performed to predict flows in noncircular ducts. The majority of these predictions as well as experiments concern, however, with square or rectangular ducts. Only a relatively few are for other cross sections such as triangular, elliptical ducts, and rod bundles. See, for example, Carlson and Irvine (1961), Aly, Trupp, and Gerrard (1978), Rapley (1982), and Demuren (1991).

Measurements made by Carlson and Irvine and Aly et al. for triangular ducts demonstrate that friction factors for these ducts based on equivalent hydraulic diameter may be lower than for circular pipe flow. Whereas the use of hydraulic diameter may cause some concern, these findings still suggest that a noncircular duct may actually be more efficient than circular pipes.

In many semi-analytic methods, it is a common practice to assume that there exists some form of similarity between a laminar and a turbulent flow for a given geometry, though the presence of the secondary flow is not usually considered. If we accept this assumption to be approximately correct and acknowledge the fact that the laminar flow friction factors for a class of ducts (super-circular ducts) are always less than those for pipe flow, there is a possibility that the turbulent friction factors in these ducts will be smaller than for circular pipe flow. On the basis of this inference, we propose to perform numerical computations for turbulent flow in this class of ducts.

To predict a turbulent flow with secondary motion, the standard form of the k-ε equations is no longer adequate and a more refined model is required. However, for the purpose of solving a fully-developed turbulent

duct flow, most of these models are closely related except for the model constants. See Kao (1994) for a more detailed discussion. Here we propose to use Speziale's model (1987) for prediction and Naot and Rodi's (1982) for comparison.

In addition to the selection of a turbulence model, we have to generate a grid and obtain finite-difference equations for computation. To this end Ryskin and Leal's method (1983) will be employed to produce an orthogonal and boundary-conforming grid, and the quadratic upstream differencing of Leonard (QUICK, 1979) will be used to solve these equations. Wall functions are also to be adopted to bridge the gap between the near-wall mesh and the surface.

Because experimental data for turbulent flow in super-circular ducts are not available at present, we can only subject the predicted results to other forms of verification, such as the scaling law of Barenblatt (1993), the decay characteristics of secondary flow when a cross section changes to a circle, and the presence of multiple vortices without imposing symmetry conditions between every vortex. Subsequent to these verification runs, regular computations are carried out for other configurations, and an attempt is made to explain the observed and predicted fact that noncircular ducts with smooth cross-sectional contours often incur higher drag than corresponding ducts with sharp corners.

2. SUPER-CIRCLE, MAPPING, AND LAMINAR FLOW COMPUTATION

A super-circle is defined to be (see Roache 1976, p. 302)

$$\left(\frac{y^*}{a^*}\right)^n + \left(\frac{z^*}{a^*}\right)^n = 1, \qquad 1 < n < \infty \tag{1}$$

where a^* is the "radius" and n is a positive number but not necessarily an integer. For instance, when $n = 2$, it represents a circle, and as $n \to \infty$, it approaches to a square. See Fig. 1 for a series of configurations with different n's. To construct a boundary-conforming orthogonal grid in a super circle, the weak-constraint form of the Ryskin and Leal method is adopted. The basic method and details are described by them and by Kao (1992), which transforms x and y to ξ and η. The ξ coordinate varies from zero at the origin to unity at the surface and is equally divided in the transformed plane. The η-coordinate corresponds approximately to the angle in a polar coordinate system, and varies from zero at the horizontal axis to $\pi/2$ at the vertical axis, which is also equally

divided. An example of such a grid is plotted in Fig. 2. This figure is for illustration; the domain for almost all computations is only an octant, extending from $\eta = 0$ to $\pi/4$.

As mentioned earlier, the predictions of turbulence friction factors in noncircular ducts have been mostly empirical until recently and are mainly based on correlations through the concept of equivalent hydraulic diameter. Since this method lacks theoretical justification, some authors (Aranovitch and Jones, among others) have proposed to include laminar flow friction factor in the process of determining equivalent Reynolds number. Although the present investigation is numerical and does not depend on correlation, one will still find the availability of laminar flow solution is useful for discussion. For this reason, we make the following digression.

The governing equation for a fully-developed incompressible laminar flow in a straight duct is

$$\frac{1}{Re}\left(\frac{\partial^2 U}{\partial y^2} + \frac{\partial^2 U}{\partial z^2}\right) + D_n = 0 \tag{2}$$

where all quantities are in dimensionless form and Re is a reference Reynolds number based on a reference velocity. See the nomenclature for its definition and Fig. 3 for other quantities. There is no secondary flow in a laminar flow, and as such U is the only nonvanishing velocity component and Eq. (2) is the governing equation. The symbol D_n refers to the dimensionless pressure gradient and is a constant. This is a linear equation and needs to be solved once for any given configuration (see Eq. (5) or (6) below).

In order to transform Eq. (2) from x and y to ξ and η, we define the following quantities:

$$y = y(\xi,\eta), \qquad z = z(\xi,\eta)$$

$$h_1^2 = y_\xi^2 + z_\xi^2, \qquad h_2^2 = y_\eta^2 + z_\eta^2, \qquad g_{12} = y_\xi y_\eta + z_\xi z_\eta = 0 \tag{3}$$

$$\frac{\partial}{\partial y} = \left(-z_\eta \frac{\partial}{\partial \xi} + z_\xi \frac{\partial}{\partial \eta}\right) \Big/ h_1 h_2, \qquad \frac{\partial}{\partial z} = \left(y_\eta \frac{\partial}{\partial \xi} - y_\xi \frac{\partial}{\partial \eta}\right) \Big/ h_1 h_2,$$

in which subscriptions ξ and η refer to partial differentiations, and the metric coefficient $g_{12} = 0$ implies orthogonality. Upon substitution of these quantities into Eq. (2) and after simplification, Eq. (2) becomes

$$\frac{1}{Re}\frac{\partial}{\partial \xi}\left(\frac{h_2}{h_1}\frac{\partial U}{\partial \xi}\right) + \frac{1}{Re}\frac{\partial}{\partial \eta}\left(\frac{h_1}{h_2}\frac{\partial U}{\partial \eta}\right) + h_1 h_2 D_n = 0 \tag{4}$$

Here U is in the axial direction and unaffected by the transformation. Notice that there is a small circle at origin in Fig. 2 to exclude the singularity, where Eq. (4) and mapping are invalid. This singularity is caused by the particular choice of ξ and η and can be removed by simply reverting it to the cartesian form locally.

It is a relatively easy matter to solve Eq. (4) numerically, for it is basically a Poisson equation. There are two special cases n = 2 (circle) and $n \to \infty$ (square, Cornish 1928) for which analytic solutions are known, whose friction factors are

$$\lambda_c = 64/\overline{\mathrm{Re}}, \qquad n = 2 \tag{5}$$

$$\lambda = 56.94/\overline{\mathrm{Re}}, \qquad n \to \infty \tag{6}$$

where $\overline{\mathrm{Re}}$ is the actual Reynolds number based on hydraulic diameter (see the nomenclature). Similar expressions can be obtained numerically for other n's. By comparing two friction factors (λ_c/λ) as shown in Table 1, the "shape" characteristics emerge,

TABLE 1.—COMPARISON OF FRICTION FACTORS

n	2	2.5	4	6	10	∞
λ_c/λ	1	1.001	1.012	1.025	1.051	1.124

which shows that these cross sections all have lower λ's.

3. GOVERNING EQUATIONS AND TRANSFORMATION

The Reynolds-averaged equations for a fully-developed incompressible turbulent flow in dimensionless forms are written first in a cartesian coordinate system.

$$\frac{\partial V}{\partial y} + \frac{\partial W}{\partial z} = 0 \tag{7}$$

$$\frac{\partial}{\partial y}(VU) + \frac{\partial}{\partial z}(WU) = D_n - \frac{\partial \overline{uv}}{\partial y} - \frac{\partial \overline{uw}}{\partial z} + \frac{1}{\mathrm{Re}}\left(\frac{\partial^2 U}{\partial y^2} + \frac{\partial^2 U}{\partial z^2}\right) \tag{8}$$

$$\frac{\partial}{\partial y}(VV) + \frac{\partial}{\partial z}(WV) = -\frac{\partial P}{\partial y} - \frac{\partial \overline{v^2}}{\partial y} - \frac{\partial \overline{vw}}{\partial z} + \frac{1}{\mathrm{Re}}\left(\frac{\partial^2 V}{\partial y^2} + \frac{\partial^2 V}{\partial z^2}\right) \tag{9}$$

$$\frac{\partial}{\partial y}(VW) + \frac{\partial}{\partial z}(WW) = -\frac{\partial P}{\partial z} - \frac{\partial \overline{vw}}{\partial y} - \frac{\partial \overline{w^2}}{\partial z} + \frac{1}{\mathrm{Re}}\left(\frac{\partial^2 W}{\partial y^2} + \frac{\partial^2 W}{\partial z^2}\right) \tag{10}$$

$$\frac{\partial}{\partial y}(Vk) + \frac{\partial}{\partial z}(Wk) = \frac{1}{Re}\frac{\partial}{\partial y}\left[\left(\frac{\nu_t}{\sigma_k} + 1\right)\frac{\partial k}{\partial y}\right] + \frac{1}{Re}\frac{\partial}{\partial z}\left[\left(\frac{\nu_t}{\sigma_k} + 1\right)\frac{\partial k}{\partial z}\right] + P - \varepsilon \tag{11}$$

$$\frac{\partial}{\partial y}(V\varepsilon) + \frac{\partial}{\partial z}(W\varepsilon) = \frac{1}{Re}\frac{\partial}{\partial y}\left[\left(\frac{\nu_t}{\sigma_\varepsilon} + 1\right)\frac{\partial \varepsilon}{\partial y}\right] + \frac{1}{Re}\frac{\partial}{\partial z}\left[\left(\frac{\nu_t}{\sigma_\varepsilon} + 1\right)\frac{\partial \varepsilon}{\partial z}\right] + C_{\varepsilon 1}\frac{P}{k}\varepsilon - C_{\varepsilon 2}\frac{\varepsilon^2}{k} \tag{12}$$

Equation (7) is the continuity equation, Eqs. (8) to (10) are momentum equations, and Eqs. (11) and (12) the transport equations for k and ε. To close this system, a turbulence closure model is needed. As stated earlier, several such models are available but they are essentially equivalent. Here we choose Speziale's model without second-order terms (see Kao 1994 for justification of neglecting these terms)

$$\nu_t = C_\mu \, Re \frac{k^2}{\varepsilon} \tag{13}$$

$$\overline{uv} = \frac{-\nu_t}{Re}\frac{\partial U}{\partial y}, \qquad \overline{uw} = -\frac{\nu_t}{Re}\frac{\partial U}{\partial z} \tag{14}$$

$$\overline{v^2} = \frac{2}{3}k - 4C_\mu \frac{\nu_t k}{Re\varepsilon}\left[\left(\frac{C_D}{12} + \frac{C_E}{3}\right)\left(\frac{\partial U}{\partial y}\right)^2 + \left(-\frac{C_D}{6} + \frac{C_E}{3}\right)\left(\frac{\partial U}{\partial z}\right)^2\right] - 2\frac{\nu_t}{Re}\frac{\partial V}{\partial y} \tag{15}$$

$$\overline{w^2} = \frac{2}{3}k - 4C_\mu \frac{\nu_t k}{Re\varepsilon}\left[\left(-\frac{C_D}{6} + \frac{C_E}{3}\right)\left(\frac{\partial U}{\partial y}\right)^2 + \left(-\frac{C_D}{12} + \frac{C_E}{3}\right)\left(\frac{\partial U}{\partial z}\right)^2\right] - 2\frac{\nu_t}{Re}\frac{\partial W}{\partial y} \tag{16}$$

$$\overline{vw} = -C_\mu C_D \frac{\nu_t k}{Re\varepsilon}\frac{\partial U}{\partial y}\frac{\partial U}{\partial z} - \frac{\nu_t}{Re}\left(\frac{\partial V}{\partial z} + \frac{\partial W}{\partial y}\right) \tag{17}$$

$$P = \frac{\nu_t}{Re}\left[\left(\frac{\partial U}{\partial y}\right)^2 + \left(\frac{\partial U}{\partial z}\right)^2\right] \tag{18}$$

There are two groups of model constants in these equations. The first group consists of the usual values for the standard k-ε model, which are $C_\mu = 0.09$, $C_{\varepsilon 1} = 1.44$, $C_{\varepsilon 2} = 1.92$, $\sigma_k = \sigma_\varepsilon = 1.225$. The second group C_D and C_E is needed for the nonlinear terms. The values chosen by Speziale are $C_D = C_E = 1.68$. In addition, we use Naot and Rodi's model for calculation and comparison as mentioned previously. No equations will, however, be given here.

With the metric coefficients given in Eq. (3), we transform Eqs. (7) to (18) into ξ-η coordinates. In this process, U is regarded as a scalar, since the transformation takes place in the y-z plane. The velocity components

V and W are, however, to be replaced by the contravariant velocity components $\hat{v}$ and $\hat{w}$ in the ξ and η directions

$$\hat{v} = y_\eta W - z_\eta V, \qquad \hat{w} = z_\xi V - y_\xi W \tag{19}$$

Thus, Eqs. (9) and (10) have to be combined to form two new momentum equations for $\hat{v}$ and $\hat{w}$. When this is done, a new set of equations emerges. All these equations, except those for $\hat{v}$ and $\hat{w}$, bear close resemblance to their counterparts. For instance, the continuity and the U momentum equations become

$$\frac{\partial \hat{v}}{\partial \xi} + \frac{\partial \hat{w}}{\partial \eta} = 0$$

$$\frac{\partial}{\partial \xi}(\hat{v}U) + \frac{\partial}{\partial \eta}(\hat{w}U) = h_1 h_2 D_n + \frac{1}{Re}\frac{\partial}{\partial \xi}\left[(\nu_t + 1)\frac{h_2}{h_1}\frac{\partial U}{\partial \xi}\right] + \frac{1}{Re}\frac{\partial}{\partial \eta}\left[(\nu_t + 1)\frac{h_1}{h_2}\frac{\partial U}{\partial \eta}\right]$$

It is not essential that Reynolds-averaged velocity components be transformed into contravariant velocity components. However, if V and W are retained, the system will contain both cartesian and contravariant velocity components, and will show up as off-diagonal terms in the SIMPLE algorithm (Patankar and Spalding, 1972) for pressure correction. Whereas Shyy and Vu (1991) suggest that these off-diagonal terms may be neglected in the computation, we prefer to work with $\hat{v}$ and $\hat{w}$ exclusively.

The above equations are in the high Reynolds number form. The following wall functions are needed to bridge the gap between the near-wall grid and the wall surface:

$$U = U_\tau \ln (E\zeta)/\kappa, \qquad \hat{w} = \sin \psi \; U_\tau \ln (E\zeta)/\kappa$$

$$k = U_\tau^2/0.3, \qquad \varepsilon = U_\tau^3/\kappa d$$

where d is the dimensionless distance in the y-z plane normal to the surface and ζ is the corresponding wall coordinate. The symbol ψ is the angle between the resultant wall shear stress and the axial direction. Since this angle is very small, the resultant stress can be approximated by U_τ as in the equation for $\hat{w}$. The above two wall functions for U and $\hat{w}$ are essentially Demuren and Rodi's form (1984), including their constants E = 0.9 and κ = 0.42, which are somewhat different from the conventional value.

4. NUMERICAL PROCEDURE

The above equations after finite differencing are to be solved by means of either the QUICK method or Spalding's hybrid method. The former is used for solving three momentum equations, while the latter for transport equations of scalar quantities. The QUICK method requires information at two grid points beyond each computational cell, which means that information has to be provided beyond the wall surface. To avoid this complication, the QUICK is implemented in the interior region two grid points away from any solid boundary, and the hybrid method is used to fill the gap between the interior and the wall. No change of computational method is, however, necessary on the other two boundaries, since these are symmetry lines. To find these solutions, we use the pentadiagonal matrix algorithm and a line-by-line sweep in both directions alternatively.

Similar to laminar flow in Section 2, the transformed equations are not valid at the origin. This singularity can be removed by again reverting to the cartesian coordinate system locally.

The pressure gradient $\partial p/\partial x$ (or D_n) in Eq. (8) for a fully-developed flow can be considered as a given constant, but the other two gradients $\partial p/\partial y$ and $\partial p/\partial z$ are unknown, have to be evaluated and rectified iteratively by the SIMPLE algorithm. To avoid the pressure-velocity decoupling, a staggered grid is adopted for $\hat{v}$ and $\hat{w}$, while permitting others to remain at the center of the control volume.

The sequence of computation in one cycle is to solve Eqs. (9) and (10) first, the pressure-correction (SIMPLE) equation next, and then Eqs. (8), (11), and (12). In the iteration process under-relaxation factors are needed. This cycle of iteration is repeated, until the absolute value of relative residuals for difference equations summed over all grid points is sufficiently small, typically in the range of 10^{-5} to 10^{-6}.

Due to the limited extent of the computational domain, a relatively fine grid distribution is feasible. For instance, the grid distribution for $\overline{\mathrm{Re}} = 6.5\times10^4$ in an octant is usually 21×41 and a finer one for higher $\overline{\mathrm{Re}}$. One of the criteria to determine the grid spacing is that the distance of the near-wall mesh is $\zeta \geq 15$ from the surface, so that wall functions can be applied properly.

5. RESULTS AND DISCUSSION

Unlike in the laminar flow case, the governing equations for a turbulent flow is nonlinear, and it is not possible to find a single solution for the entire range of the Reynolds numbers. The flow field in a given super-circular duct for each Reynolds number must be computed individually. Thus, a fairly large amount of

computations is needed to cover a moderate range of Reynolds numbers for several configurations. The configurations to be considered are n = 2.5, 4, and 6.

We begin with a duct with n = 2.5. Since this configuration differs from a circle by a small amount, one may doubt whether a secondary flow actually exists and, if it exists, what will be its intensity. In the absence of experimental data, we can only provide indirect verifications. Three procedures are to be employed. First, we perform the computation in a half domain instead of a usual octant to see whether a similar pattern emerges. Secondly, the obtained result is to be subject to an accuracy check by means of a scaling law. Finally, we examine the decay process to see whether the secondary flow will vanish, if the cross section changes to a circle.

5.1 Flow Field in a Half Domain

The computational domain for regular calculations is an octant with symmetry conditions imposed along two "radii" (OA and OB in Fig. 3). The calculated flow field in such a domain shows clearly the presence of secondary flow. However, since symmetry conditions are imposed on both sides, one may still ask the question whether the secondary flow can subsist without these conditions. To remove this doubt, a second set of computation was made in which the same numerical procedure was applied except that the computational domain was then enlarged to include one-half of the cross section and symmetry conditions were imposed only along the cross-sectional symmetry line. We plot the obtained secondary flow velocity vectors after 1300 cycles of iteration in Fig. 4 to show that there are still four cells of clearly defined recirculatory motions. This demonstration suggests that the use of an octant is legitimate and a secondary flow with eight recirculatory zones is likely to be observed experimentally in a duct whose cross section differs from a circle by only a small amount (n = 2.5).

5.2 Scaling law of Barenblatt

We use this scaling law mainly to examine the accuracy of streamwise velocity components. Although it resembles the conventional power-law relationship, it is formulated differently and has the form

$$\phi^{\alpha} = C\zeta, \qquad \alpha = 2 \ln \bar{R}e/3 \tag{20}$$

where $\phi = U^*/U_\tau^*$, C is a constant, and ζ is the wall coordinate. This expression is valid in the intermediate interval of the shear flow and implies that the graph ϕ^{α} plotted against ζ is a straight line. An intermediate interval is defined to be a range, which is sufficiently large in comparison with the viscous sublayer but small

with respect to the duct width. Strictly speaking, Eq. (20) is good only for parallel flows. Thus, using it for the present problem is merely an approximation with U^* being only one component of the resultant. For this reason, the plotted graph may not be a truly straight line. However, even an approximately straight line may be encouraging. The coefficient α in Eq. (20) is a dimensionless empirical constant (Barenblatt and Prostokishin, 1993).

Plotted in Fig. 5 are four ϕ^α graphs for configurations n = 2.5 and 6. Only points within the intermediate interval are shown. It appears that groups of symbols along $\theta \approx 15°$ form nearly perfect straight lines, but those along $\theta = 0$ are somewhat curved. A possible explanation is that the secondary velocity components at the center of vortex ($\theta \approx 15°$) are nearly parallel to the surface (Fig. 4) and thus have less effect on the U^* component, whereas those along the symmetry line are directed away from the surface, which makes the streamwise flow less parallel. Note also that the exponent α in Eq. (20) is a large number; a small departure from the correct value will cause the graph to bend.

5.3 Decay of Secondary Motion

A closer look at the secondary motion reveals that its intensity in a n = 2.5 duct is actually higher than that in a square duct at a corresponding Reynolds number. This is in contrary to our intuition. Consequently, we subject our computation to another test by changing the cross section from n = 2.5 to 2 (circle) and observing the decaying process of the secondary flow. This has to take place, if the present computational procedure is correct, owing to the fact that in a circular pipe the difference of normal Reynolds stresses $\overline{v^2} - \overline{w^2}$ is zero and there is no mechanism to subsist a secondary motion. The process will, however, be slow, since it can only be annihilated through viscous dissipation.

To illustrate this process, we plot the initial velocity profile in Fig. 6(a) and the corresponding velocity field based on Naot and Rodi's model after 6000 cycles of iterations in Fig. 6(b). Whereas the remanence of the secondary motion is visible, most velocity vectors have essentially vanished and cannot be discerned in the present scale. (An open arrow head represents merely a direction, obtainable no matter how small the velocity vector is as long as the ratio of two components are correct, and the stem is the magnitude). As expected, the decay of the secondary motion is much faster in the beginning than at the later stage, and velocities slow down first near the surface. For instance, the flow pattern after 3000 iterations is already fairly similar to that in

Fig. 6(b). When the secondary flow completely subsides, the wall shear stresses in a circular pipe should be uniform everywhere and the friction factors agree with the Blasius or Prandtl formula. No complete subsidence is achieved in Fig. 6(b) especially near the plane of symmetry, and the wall shear stresses are not exactly uniform. As a result, the predicted friction factor is somewhat higher than the Blasius formula. This concludes our test for n = 2.5.

5.4 Wall Shear Stress

Two groups of predicted wall shear stress distributions are plotted in Fig. 7 against the dimensionless distance along the wall. (Wall distances are made dimensionless by referring to the duct "radius," which is a constant, and therefore the lengths for different configurations are different.) The top group is for flows at relatively low Reynolds numbers, while those in the lower group are for higher Reynolds numbers. The purpose here is to demonstrate that cross-sectional configurations in terms of dimensionless quantities do not seem to have much influence on the stress distribution. As n increases, it becomes more similar to the distribution in a square duct. In particular, it increases first, reaches the maximum at the middle of the vortex and then decreases. For this reason, we also plot experimental data of a square duct with similar Reynolds numbers. The resemblance is apparent.

The wall stresses at one end of the vortex are always less than at the other end. This is likely due to the fact that the "recirculating" motion of the secondary flow at one side of the vortex ($S^* = 0$ in Fig. 7) is directed away from the surface, which lifts the viscous layer and decreases the shear stress, whereas the motion at the other end is directed towards the surface, which compresses the viscous layer and, in turn, increases the wall stress. The wall shear stresses for $n \geq 6$ increase in the first half of the vortex but bend downward in the second half. The reason for this is perhaps as follows. As n increases, corners begin to form, and when n is 6 or greater, they become relatively "sharp." A sharp corner has two walls surrounding the flow, which causes the streamwise velocity to slow down in its vicinity and lowers the shear stress.

5.5 Friction Factors

One may envision in a noncircular duct that there are two competing forces at play. One is the shape advantage inherent with most noncircular cross sections including various triangles (Carlson and Irvine) and the other is the loss induced by secondary flow showing up in the form of drag increase. When the former dominates

the latter as in triangular ducts, where the shape advantage can be as much as 20 percent over a circular pipe, the friction factors become less than those for circular pipes (see measurements taken by Carlson and Irvine and Fig. 8). If these two forces are somehow in balance as in a square or rectangular duct, its friction factors agree with Blasius' empirical equation fairly well. However, the shape advantage for a super-circular duct is relatively small as compared with a square duct and yet the secondary flow is still strong. Thus, the latter becomes more dominant and the friction factors are higher than both (see Fig. 8).

If one considers a circle to be a curve fit for a square, which contacts the latter at four points, the corresponding shape for a rectangle is then an ellipse with a like aspect ratio. This geometric equivalence cannot, however, be translated into a friction factor equivalence, since in contrast to circular pipes the friction factors for elliptical ducts as measured by Cain and Duffy (1971) are considerably higher than those for rectangular duct (see Fig. 8). (Friction factors for rectangular ducts, though not shown in Fig. 8 to avoid cluttering, are approximately the same as for circular pipes) The reason is believed to be that a circular pipe, though inferior in shape characteristics, is absent with secondary flow, which makes it possible to have similar friction factors to a square duct, whereas in an elliptical duct the omnipresent secondary flow induces an additional loss and leads to higher friction factor than for rectangular ducts. A similar situation is believed to exist for super-circular ducts, which unlike a circular pipe accommodates secondary motion and suffers from higher drag than for a square duct.

To extend this observation further, one may even conjecture that a duct with a smooth contoured cross section such as a circle, super-circle, ellipse or super-ellipse, cannot transport fluid more efficiently than a corresponding duct whose cross section has sharp corners. This includes both laminar and turbulent flows. Note that this is merely an observation and a complete justification is perhaps not attainable as our understanding about secondary flow losses is still inadequate (Hawthorne, 1990).

6. CONCLUDING REMARKS

Since there exists some evidence insofar as friction factors are concerned that noncircular ducts may be more efficient in transport fluid flows than circular pipes, a study was made to numerically investigate turbulent flow properties in ducts of super-circular cross sections. In the absence of available experimental data to test the validity of predicted results, we can only subject them to other forms of verification, such as an accuracy check

by a scaling law or observing the decaying process of the secondary flow as the cross section changes from a noncircular shape to a circle. The evidence seems to suggest that the predictions are correct. A somewhat unexpected result is that the predicted friction factors for super-circular ducts are higher than those for circular or square ducts. However, after a close examination of several different classes of configurations it seems that a noncircular duct with a smooth cross-sectional contour is likely to be less efficient than a circular pipe, but if the cross section is not smooth and has sharp corners, it may be as efficient as or more efficient that a circular pipe.

REFERENCES

Aly, A.M.M., Trupp, A.C., and Gerrard, A.D., 1978. Measurements and prediction of fully developed turbulent flow in an equilateral triangular duct. *J. Fluid Mech.*, **85**, 57–83.

Aranovitch, E., 1971. A method for determination of the local turbulent friction factor and heat transfer coefficient in generalized geometries. *ASME J. Heat Transfer*, **93**, 61–68.

Barenblatt, G.I., 1993. Scaling laws for fully developed turbulent shear flows. Part 1. Basic hypothesis and analysis. *J. Fluid Mech.*, **248**, 513–520.

Barenblatt, G.I. and Prostokishin, V.M., 1993. Scaling law for fully developed turbulent shear flows. Part 2. Processing of experimental data. *J. Fluid Mech.*, **248**, 521–529.

Cain, D. and Duffy, J., 1971. An experimental investigation of turbulent flow in elliptical ducts. *Int. J. Mech. Sci.*, **13**, 451–459.

Carlson, L.W. and Irvine, T.F., 1961. Fully developed pressure drop in triangular shaped ducts. *J. Heat Transfer*, **83C**, 441–444.

Cornish, R.J., 1928. Flow in a pipe of rectangular cross-section. *Proc. Roy. Soc. A.*, **120**, 691–700.

Demuren, A.O., 1991. Calculation of turbulence-driven secondary motion in ducts with arbitrary cross section. *AIAA J.*, **29**, 531–537.

Demuren, A.O. and Rodi, W., 1984. Calculation of turbulence-driven secondary motion in non-circular ducts. *J. Fluid Mech.*, **140**, 189–222.

Gessner, F.B. and Emery, A.F., 1979. The numerical prediction of developing turbulent flows in rectangular ducts. *Proceedings, Turbulent Shear Flow 2*, London, England.

Hartnett, J.P., Koh, J.C.Y., and McComas, S.T., 1962. A comparison of predicted and measured friction factors for turbulent flow through rectangular ducts. *ASME J. Heat Transfer*, **84**, 82–88.

Hawthorne, W., 1990. Loss mechanism in secondary flow. Some unanswered questions in fluid mechanics. Compiled by L.M. Trefethen and R.L. Panton. *Appl. Mech. Rev.*, **43**(8), 153–169.

Jones, O.C., 1976. An improvement in the calculation of turbulent friction in rectangular ducts. *ASME J. Fluids Eng.*, **98**, 173–181.

Kao, H.C., 1992. Some aspects of bifurcation structure of laminar flow in curved ducts. *J. Fluid Mech.*, **243**, 519–539.

Kao, H.C., 1994. Some remarks about modeling for turbulent flow in a square duct. Submitted for publication.

Leonard, B.P., 1979. A stable and accurate convective modeling procedure based on quadratic upstream interpolation. *Comput. Meth. Appl. Mech. Eng.*, **19**, 59–98.

Myong, H.K., 1991. Numerical investigation of fully developed turbulent fluid flow and heat transfer in a square duct. *Int. J. Heat and Fluid Flow*, **12**, 344–352.

Naot, D. and Rodi, W., 1982. Calculation of secondary currents in channel flow. *ASCE J. Hydraul. Div.*, **108**(HY8), 948–967.

Patankar, S.V. and Spalding, D.B., 1972. A calculation procedure for heat, mass and momentum transfer in three-dimensional parabolic flows. *Int. J. Heat Mass Transfer*, **15**, 1787–1806.

Rapley, C.W., 1982. The simulation of secondary flow effects in turbulent non-circular passage flows. *Int. J. Num. Meth. in Fluids*, **2**, 331–347.

Roache, P.J., 1976. *Computational Fluid Dynamics*, Hermosa Publishers, Albuquerque, NM.

Ryskin, G. and Leal, L.G., 1983. Orthogonal mapping. *J. Comput. Phys.*, **50**, 71–100.

Shyy, W. and Vu, T.C., 1991. On the adoption of velocity variable and grid system for fluid flow computation in curvilinear coordinates. *J. Comput. Phys.*, **92**, 82–105.

Speziale, C.G., 1987. On nonlinear k-ℓ and k-ε models of turbulence. *J. Fluid Mech.*, **178**, 450–475.

TABLE 1.—COMPARISON OF FRICTION FACTORS

n	2	2.5	4	6	10	∞
λ_c/λ	1	1.001	1.012	1.025	1.051	1.124

FIGURE CAPTIONS

Fig. 1 Depiction of super circles of various exponents.

Fig. 2 41×41 orthogonal grid (n = 6, equal interval in ξ-η plane).

Fig. 3 Coordinate system, velocity components and computational domain.

Fig. 4 Vector plot of secondary motion at every other mesh point (n = 2.5, $\overline{Re} = 5.14\times10^4$).

Fig. 5 Graphs of Barenblatt's scaling law (n = 2.5, and 6, $\overline{Re} = 2.18\times10^5$).

Fig. 6 Secondary velocity fields in a circular pipe plotted at every other point in radial direction.
(a) Initial profile. (b) Profile after 6000 cycles of iteration at $\overline{Re} = 4.83\times10^4$.

Fig. 7 Wall shear stress distributions along duct wall.

Fig. 8 Comparison of friction factors for circular, square, triangular, elliptical and super-circular ducts.

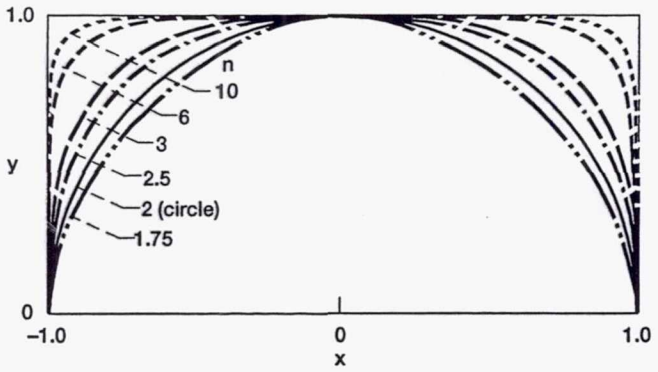

Figure 1.—Depiction of super-circles of various exponents.

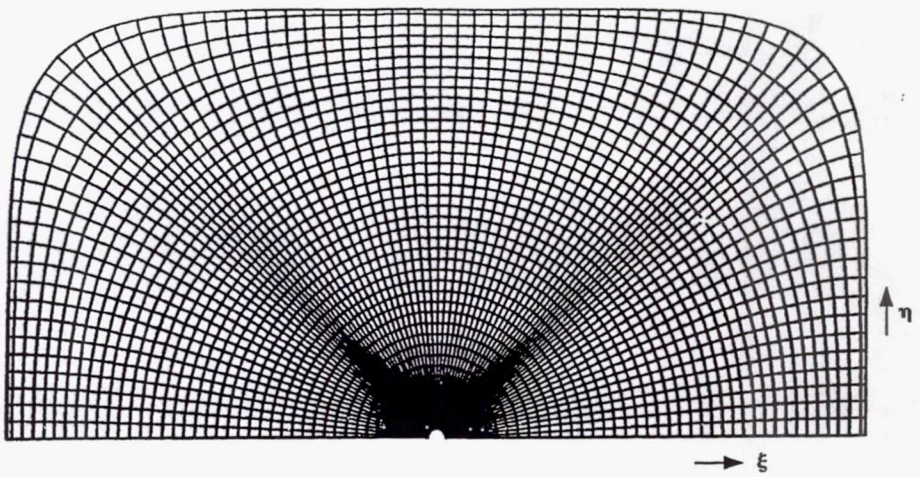

Figure 2.—41x41 Orthogonal grid (n = 6, equal interval in ξ–η plane).

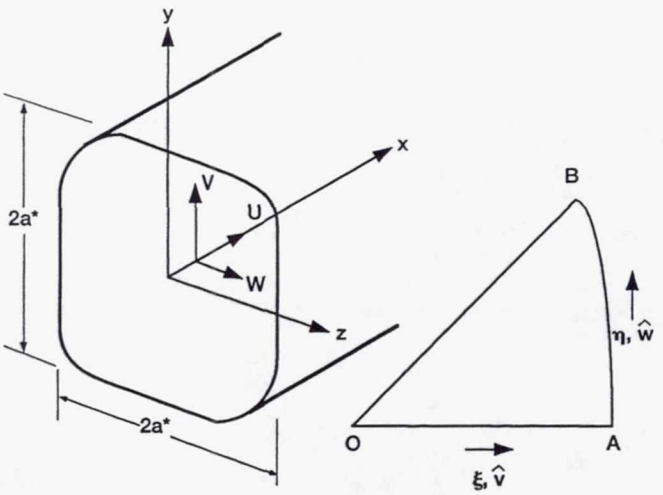

Figure 3.—Coordinate system, velocity components and computational domain.

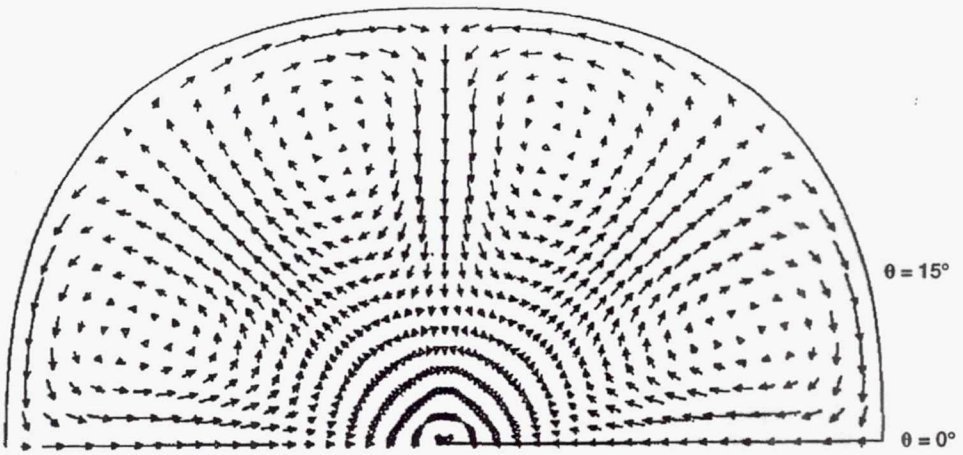

Figure 4.—Vector plot of secondary motion at every other mesh point (n = 2.5, $\overline{R}_e = 5.14 \times 10^4$).

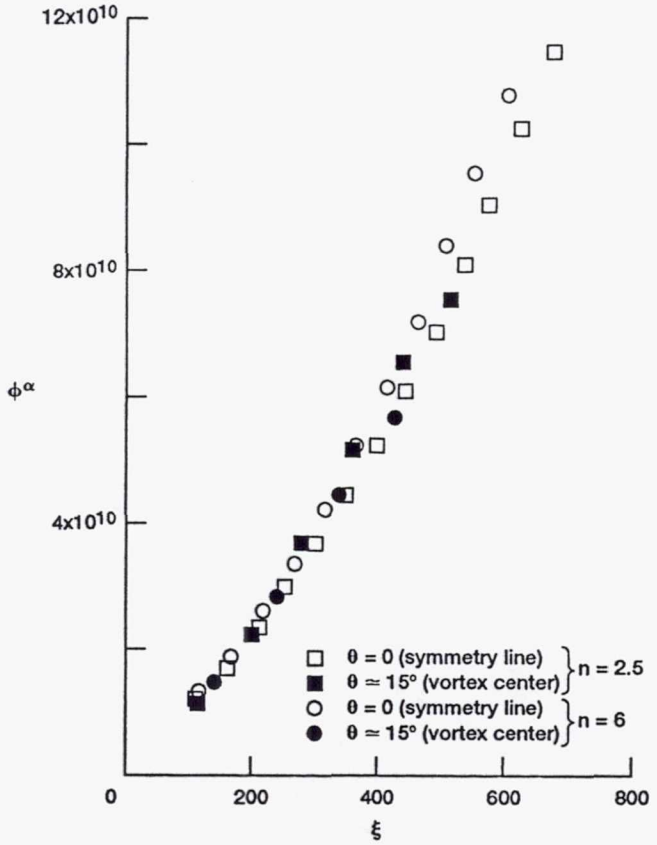

Figure 5.—Graphs of Barenblatt's scaling law (n = 2.5 and 6, $\bar{R}_e = 2.18 \times 10^5$).

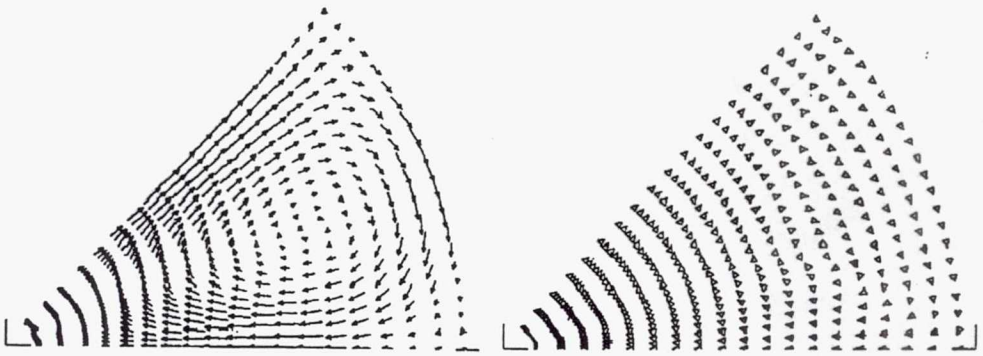

Figure 6.—Secondary velocity fields in a circular pipe plotted at every other point in radial direction. (a) Initial profile. (b) Profile after 6000 cycles of iteration at $\overline{R}_e = 4.83 \times 10^4$.

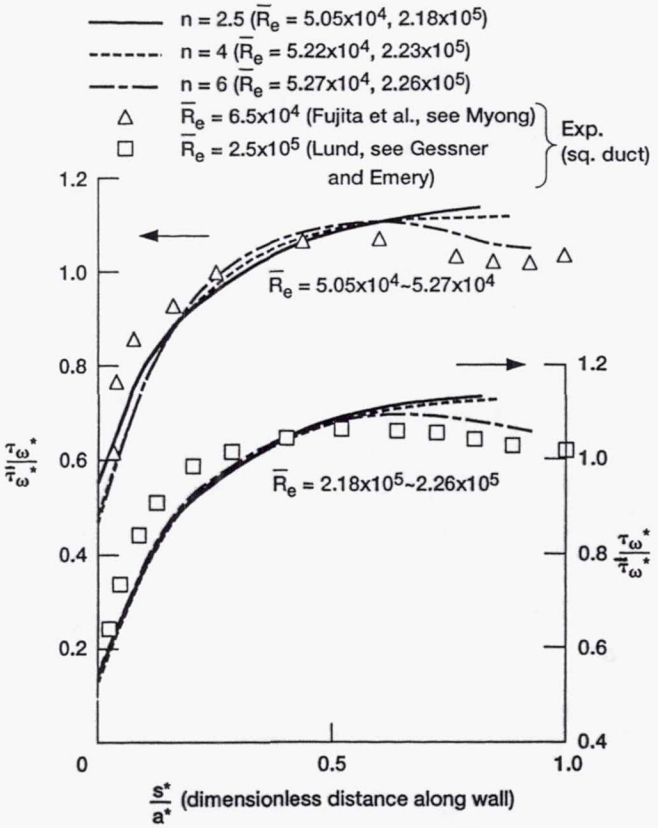

Figure 7.—Wall shear stress distributions along duct wall.

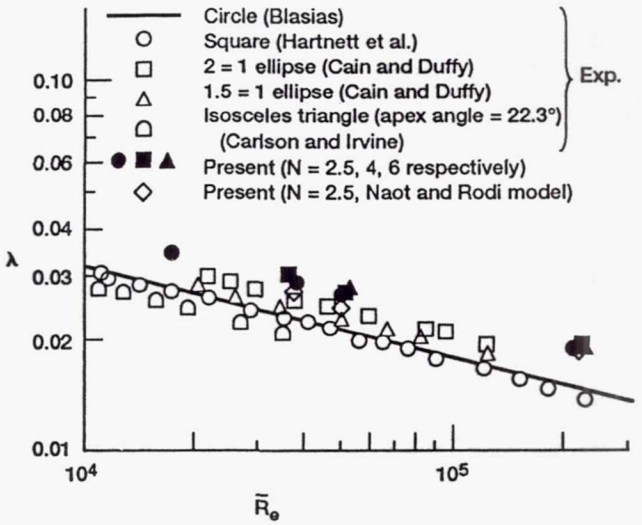

Figure 8.—Comparison of friction factors for circular, square, triangular, elliptical and super-circular ducts.